

THE EUROPEAN LARGE-AREA INFRARED SPACE OBSERVATORY SURVEY V: A *BeppoSAX* HARD X-RAY SURVEY OF THE S1 REGION

D. M. ALEXANDER,^{1,2} F. LA FRANCA,³ F. FIORE,⁴ X. BARCONS,⁵ P. CILIEGI,⁶ L. DANESE,¹ R. DELLA CECA,⁷
A. FRANCESCHINI,⁸ C. GRUPPIONI,⁸ G. MATT,³ I. MATUTE,³ S. OLIVER,⁹ F. POMPILIO,¹ A. WOLTER,⁷
A. EFSTATHIOU,¹⁰ P. HÉRAUDEAU,¹¹ G. C. PEROLA,³ M. PERRI,¹² D. RIGOPOULOU,¹³
M. ROWAN-ROBINSON,¹⁰ AND S. SERJEANT¹⁰

Received 2000 September 15; accepted 2001 January 30

ABSTRACT

We present *BeppoSAX* observations of the southern S1 region in the European Large-Area *Infrared Space Observatory* (ISO) Survey (ELAIS). These observations cover an area of ~ 1.7 deg² and reach an on-axis (~ 0.7 deg²) 2–10 keV (hard X-ray, or HX) sensitivity of $\sim 10^{-13}$ ergs s⁻¹ cm⁻². This is the first HX analysis of an ISOCAM survey. We detect nine sources with a signal-to-noise ratio $\text{SNR}_{\text{HX}} > 3$, four additional sources with a 1.3–10 keV (total X-ray, or *T*) $\text{SNR}_T > 3$, and two additional sources that seem to be associated with QSOs having $\text{SNR}_T > 2.9$. The number densities of the $\text{SNR}_{\text{HX}} > 3$ sources are consistent with the *ASCA* and *BeppoSAX* log *N*–log *S* functions. Six *BeppoSAX* sources have reliable ISOCAM 15 μm counterparts within $\sim 60''$. All these ISOCAM sources have optical counterparts of $R < 20$ mag. Five of these sources have been previously optically classified, four as QSOs and one as a broad absorption line (BAL) QSO at $z = 2.2$. The remaining unclassified source has X-ray and photometric properties consistent with those of a nearby Seyfert galaxy. One further HX source has a 2.6σ ISOCAM counterpart associated with a galaxy at $z = 0.325$. If this ISOCAM source is real, the HX/MIR properties suggest either an unusual QSO or a cD cluster galaxy. We have constructed MIR and HX spectral energy distributions to compute the expected HX/MIR ratios for these classes of objects up to $z = 3.2$ and assess the HX/MIR survey depth.

The BAL QSO has an observed X-ray softness ratio and HX/MIR flux ratio similar to those of QSOs but different from those found for low-redshift BAL QSOs. This difference can be explained in terms of absorption, and it suggests that high-redshift BAL QSOs should be comparatively easy to detect in the HX band, allowing their true fraction in the high-redshift QSO population to be determined. The QSOs cover a wide redshift range ($0.4 < z < 2.6$) and have HX/MIR flux ratios consistent with those found for nearby *IRAS* and optically selected Palomar-Green QSOs. This suggests that MIR-selected QSOs of $R < 20$ mag come from the same population as optically selected QSOs. We confirm this with a comparison of the *B*/MIR flux ratios of MIR and blue-band-selected QSOs.

Subject headings: cosmology: observations — galaxies: active — infrared: galaxies — surveys — X-rays: galaxies

1. INTRODUCTION

Unified models of active galactic nuclei (AGNs) propose that all types of AGNs are fundamentally the same,

¹ International School for Advanced Studies, SISSA, via Beirut 2-4, I-34014 Trieste, Italy.

² Present address: Department of Astronomy and Astrophysics, Pennsylvania State University, 525 Davey Laboratory, University Park, PA 16802; davo@astro.psu.edu.

³ Dipartimento di Fisica, Università degli Studi “Roma Tre,” via della Vasca Navale 84, I-00146 Roma, Italy.

⁴ Osservatorio Astronomico di Roma, via Frascati 33, Monteporzio, Italy.

⁵ Instituto de Física de Cantabria (Consejo Superior de Investigaciones Científicas-Universidad de Cantabria), 39005 Santander, Spain.

⁶ Osservatorio Astronomico di Bologna, via Ranzani 1, Bologna, Italy.

⁷ Osservatorio Astronomico di Brera, via Brera 28, Milano, Italy.

⁸ Osservatorio Astronomico di Padova, Vicolo dell’Osservatorio 5, Padova, Italy.

⁹ Astronomy Centre, CPES, University of Sussex, Falmer, Brighton, UK.

¹⁰ Astrophysics Group, Imperial College of Science, Technology, and Medicine, Prince Consort Road, London, UK.

¹¹ Max-Planck-Institut für Astronomie (MPIA), Königstuhl 17, Heidelberg D-69117, Germany.

¹² *BeppoSAX* Science Data Center, ASI, Via Corcolle 19, Roma, Italy.

¹³ Max-Planck-Institut für extraterrestrische Physik (MPE), Postfach 1603, Garching D-85740, Germany.

although the presence of a dusty molecular torus prevents the observation of the broad line region for particular lines of sight. In this picture type 1 AGNs (e.g., Seyfert 1’s, QSOs) are those for which the nucleus can be directly observed, while in type 2 AGNs (e.g., Seyfert 2’s) the nucleus is obscured by the torus (see, e.g., Lawrence & Elvis 1982 and Antonucci 1993). Strong support for this model has been given by X-ray, near-IR, and mid-IR observations showing that type 2 AGNs are characterized by strong absorption, while type 1 AGNs are relatively unabsorbed (Turner et al. 1997; Alonso-Herrero, Ward, & Kotilainen 1997; Maiolino et al. 1998; Clavel et al. 2000). In this framework the infrared radiation is interpreted in terms of thermal emission from hot dust grains heated by the high-energy central source emission (optical to X-ray continuum; see, e.g., Granato, Danese, & Franceschini 1997).

Barcons et al. (1995, hereafter B95) investigated the 12 μm to hard X-ray (HX, 2–10 keV) flux ratios of a sample of nearby AGNs and galaxies using *IRAS* and *HEAO1* A-2 observations. They found that type 1 AGNs have larger HX/12 μm flux ratios than type 2 AGNs, while normal galaxies have very weak HX emission. This implies high column densities [$\log(N_{\text{H}}) > 22$ cm⁻²] in the type 2 objects, supporting the basic unified model hypothesis. The B95 study was necessarily restricted to nearby objects. The

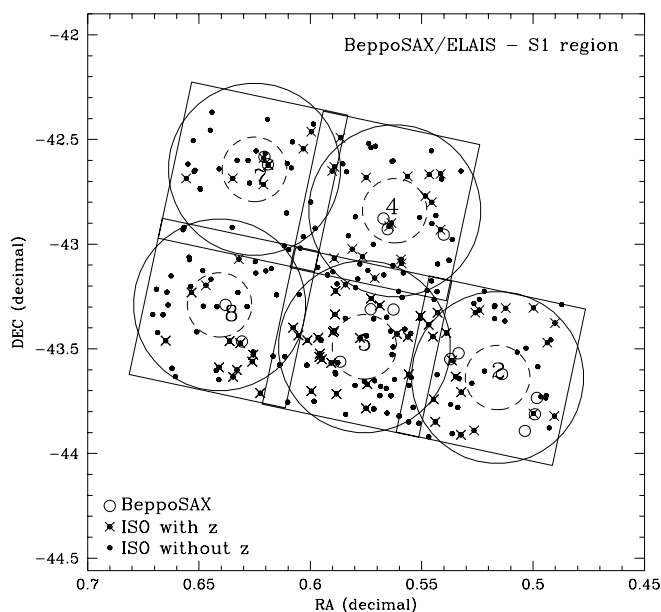


FIG. 1.—Observed ELAIS S1 subfields overlaid with the ISOCAM 15 μm sources (points), classified sources (crosses; La Franca et al. 2001, in preparation; Gruppioni et al. 2001, in preparation) and *BeppoSAX* detected sources (small open circles). The overall field of view of the MECS instrument ($\sim 50'$ diameter; large open circles) and the highest-sensitivity regions (dashed circles) are shown.

investigation of this flux ratio to deeper fluxes and higher redshifts will probe the properties of luminous sources, such as QSOs and broad absorption line QSOs (BAL QSOs), and provide clues to the constancy of AGN activity in the universe.

The *ASCA* and *BeppoSAX* X-ray satellites have been successful in determining the HX properties of AGNs and have resolved $\sim 30\%$ of the HX background into discrete sources, mostly type 1 and type 2 AGNs (see, e.g., Ueda et al. 1998, 1999, Cagnoni, Della Cecca, & Maccacaro 1998, Fiore et al. 1999, and Akiyama et al. 2000). The recent launch of the *Chandra* and *XMM-Newton* X-ray satellites has now made it possible to probe to fainter fluxes at HX energies. Recent *Chandra* observations (see, e.g., Mushotzky et al. 2000, Fiore et al. 2000a, Brandt et al. 2000, Giacconi et al. 2001, and Hornschemeier et al. 2000) have uncovered a number of HX-emitting, though apparently optically normal, galaxies. The HX slopes of the sources are sufficiently hard that, when combined with the HX-emitting

AGN sources, they can account for more than 75% of the HX background (see, e.g., Mushotzky et al. 2000, Giacconi et al. 2001, and Hornschemeier et al. 2001). Comparisons with deep submillimeter surveys have shown that these HX sources are almost always unassociated with submillimeter sources (see, e.g., Hornschemeier et al. 2000, Severgnini et al. 2000, Fabian et al. 2000, and Barger et al. 2001), which instead appear to be star-forming systems. Because of the expected association between HX and MIR emission, a closer correlation should be found in the mid-IR band.

We present here *BeppoSAX* hard X-ray observations of the S1 region of the European Large Area *ISO* Survey (ELAIS) at 15 μm . ELAIS (Oliver et al. 2000) was the largest program undertaken by *ISO* and, covering an area of $\sim 12 \text{ deg}^2$, it will be the largest 15 μm (Serjeant et al. 2000) and 90 μm (Efstathiou et al. 2000) survey until *SIRTF* and *FIRST* come into play. In this paper we focus on observations in the southern S1 region. In addition to the *ISO* observations, this region has been covered in the *U*, *B*, *R*, and *I* (La Franca et al. 2001, in preparation; Héraudeau et al. 2001, in preparation) optical bands and the 1.4 GHz radio (Gruppioni et al. 1999) band. Selected objects have been observed spectroscopically in the optical (La Franca et al. 2001, in preparation; Gruppioni et al. 2001, in preparation) and photometrically in the near-IR (Héraudeau et al. 2001, in preparation). The field of view of the *BeppoSAX* medium-energy concentrator spectrometer, or MECS (25' of radius; Boella et al. 1997a, 1997b), matches well with that of the ELAIS subfields, covering a considerably larger area than both *Chandra* and *XMM-Newton* (see Fig. 1). It is thus ideal for a shallow X-ray survey of ELAIS fields. Throughout this paper $H_0 = 50 \text{ km s}^{-1}$, $\Lambda = 0$, and $q_0 = 0.5$ are used.

2. OBSERVATIONS

The *BeppoSAX* observations were taken with both the low-energy concentrator spectrometer (LECS) and MECS. The LECS observations are not considered here because of their lower sensitivity and much poorer point-spread function (PSF) below 2 keV.

The MECS observations (Boella et al. 1997b), from 1.3 to 10 keV, cover five of the nine subfields in the S1 region of ELAIS (see Fig. 1). The total area covered is $\sim 1.7 \text{ deg}^2$, although the sensitivity of MECS varies with off-axis distance, with the most sensitive observations covering 0.7 deg^2 . The on-source exposure time for these five pointings was on average $\sim 36 \text{ ks}$, corresponding to a flux limit of $\sim 10^{-13} \text{ ergs s}^{-1} \text{ cm}^{-2}$ on-axis (see Table 1).

TABLE 1

BeppoSAX MECS OBSERVATIONS

Field (1)	Center Position (2)	Exposure Time (ks) (3)	Date (4)	X-offset (deg) (5)	Y-offset (deg) (6)
S1.2.....	0 30 57.3 -43 38 12.9	34.0	1999 Dec 15	0.0222	0.0040
S1.4.....	0 33 43.6 -42 50 25.0	33.1	1999 Dec 20
S1.5.....	0 34 32.6 -43 29 24.0	36.1	1999 Dec 19
S1.7.....	0 37 30.3 -42 38 38.2	43.2			
		27.8	1999 Jul 18	-0.0206	0.0041
		15.4	1999 Dec 19
S1.8.....	0 38 26.7 -43 17 23.7	31.2	1999 Jul 17	0.0000	0.0062

NOTES.—Col. (1): ELAIS region. Col. (2) Uncorrected X-ray field center position (J2000). Units of right ascension are hours, minutes, and seconds, and units of declination are degrees, arcminutes, and arcseconds. Col. (3): Observation exposure time. Col. (4): Date of observation. Col. (5): R.A. correction. Col. (6): Decl. correction. See § 2 for discussion of cols. (5) and (6).

The *BeppoSAX* positional accuracy is dependent on many factors (see Fiore et al. 2000b for details), leading to a 95% error radius of 60" at off-axis distances less than 12' and 1.5 at greater distances. Slightly better accuracies have been achieved in those fields where we have been able to identify more than one source at another wavelength and to perform a positional shift of the X-ray sources to match the more accurate optical positions (see Table 1).

3. DATA

3.1. ELAIS Data

As discussed in the introduction, the characteristics of the ELAIS selection and the infrared counts have been presented by Oliver et al. (2000) and Serjeant et al. (2000). The survey has covered an area of $\sim 12 \text{ deg}^2$ down to $\sim 1 \text{ mJy}$ in the $15 \mu\text{m}$ LW3 filter (referred to here as MIR; Cesarsky et al. 1996). In this paper we focus on observations in the S1 region centered at $\alpha(2000) = 00^{\text{h}}34^{\text{m}}44^{\text{s}}.4$, $\delta(2000) = -43^{\circ}28'12''$, which covers an area of about $2^{\circ} \times 2^{\circ}$. About 100 sources in the preliminary analysis of ELAIS (Serjeant et al. 2000) down to $R \sim 20.5 \text{ mag}$ have been spectroscopically identified during three spectroscopic identification campaigns in 1998 (La Franca et al. 2001, in preparation; Gruppioni et al. 2001, in preparation).

3.2. *BeppoSAX* Data

The *BeppoSAX* observations were cleaned and linearized using the Science Data Center (SDC) on-line analysis. The

MECS2 and MECS3 images were co-added together and binned by a factor of 2. Source detection was performed using XIMAGE with the interactive routine SOSTA. When measuring the counts of a source a box of 13 pixels² (each pixel corresponds to 8") was used. This was found to maximize the signal-to-noise ratio. As the PSF is much larger than the positional uncertainty, the effect on the flux from poor centroiding with weak sources is negligible. The net counts were automatically corrected for vignetting, sampling dead time, and the PSF. For each source the background was measured in large apertures at nearby orthogonal sky positions.

The conversion from counts to fluxes was determined using a power law of $\alpha = 0.7$ ($f_{\nu} \propto \nu^{-\alpha}$). We experimented with a range of column densities [$20 < \log(N_{\text{H}}) < 23$] but found small differences ($\sim 10\%$) in the conversion factors as compared with the uncertainty in the counts of the X-ray sources and the flux uncertainties of the MIR sources, which are of the order of 30% (Serjeant et al. 2000). The overall conclusions are not affected by these uncertainties.

We initially found 13 sources at the $\text{SNR} > 3$ Poisson level in the 1.3–10 keV (*T*) or 2–10 keV (*HX*) band, although two of these sources could be unreliable because of possible source confusion (sources s2 and s4), and they are included in a supplementary table (see Tables 2 and 3 and Fig. 1). Based on the source box size, we would expect less than one spurious source due to background fluctuations. Considering the relatively small cosmic volume sampled, the

TABLE 2
BeppoSAX SOURCES

Object (1)	X-Ray Position (2)	SNR_T (3)	Counts _{HX} (4)	SNR_{HX} (5)	f_{HX} ($\times 10^{-13} \text{ ergs s}^{-1} \text{ cm}^{-2}$) (6)	Softness (7)
1	0 30 13.1 –43 53 31.3	5.1	5.7 ± 1.2	4.8	5.3 ± 1.2	-0.11 ± 0.28
2	0 30 50.2 –43 37 15.4	3.6	1.5 ± 0.4	3.7	1.4 ± 0.4	-0.51 ± 0.39
3	0 32 13.8 –43 32 56.9	3.9	2.2 ± 0.7	3.4	2.0 ± 0.7	0.32 ± 0.44
4	0 32 24.3 –42 57 15.6	3.1	2.7 ± 1.0	2.8	2.5 ± 1.0	-0.39 ± 0.56
5	0 33 45.7 –43 18 44.7	3.9	2.7 ± 0.7	3.6	2.5 ± 0.7	0.18 ± 0.35
6	0 34 01.7 –42 52 38.6	2.9	1.3 ± 0.4	3.3	1.2 ± 0.4	-0.37 ± 0.47
7	0 34 22.3 –43 18 38.3	2.0	1.5 ± 0.5	3.1	1.4 ± 0.5	-0.46 ± 0.36
8	0 35 11.7 –43 33 42.2	8.7	4.0 ± 0.6	6.8	3.7 ± 0.6	0.59 ± 0.14
9	0 37 08.4 –42 37 07.6	6.5	2.4 ± 0.4	6.0	2.2 ± 0.4	0.31 ± 0.20
10.....	0 37 14.3 –42 34 55.6	5.5	1.9 ± 0.4	5.0	1.8 ± 0.4	0.22 ± 0.26
11.....	0 37 50.5 –43 27 53.1	3.3	1.8 ± 0.6	2.9	1.7 ± 0.6	-0.08 ± 0.43

NOTES.—Col. (1): *BeppoSAX* source number. Col. (2): *BeppoSAX* position (J2000); see text for positional accuracy. Units of right ascension are hours, minutes, and seconds, and units of declination are degrees, arcminutes, and arcseconds. Col. (3): Total X-ray (1.3–10 keV) SNR. Col. (4): Hard X-ray (2–10 keV) counts. Col. (5): Hard X-ray SNR. Col. (6): Hard X-ray flux. Col. (7): Softness ratio $(S-H)/(S+H)$; see § 4.2.

TABLE 3
SUPPLEMENTARY *BeppoSAX* SOURCES

Object (1)	X-Ray Position (2)	SNR_T (3)	Counts _{HX} (4)	SNR_{HX} (5)	f_{HX} ($\times 10^{-13} \text{ ergs s}^{-1} \text{ cm}^{-2}$) (6)	Softness (7)	Reason for Inclusion (8)
s1	0 29 57.1 –43 48 44.3	2.9	2.2 ± 0.9	2.4	2.0 ± 0.9	-0.58 ± 0.43	$\text{SNR}_T = 2.9$ but 33" from QSO
s2.....	0 32 00.4 –43 31 14.9	3.8	1.3 ± 0.5	2.5	1.2 ± 0.5	0.46 ± 0.42	Close to source 3, maybe one source
s3.....	0 33 55.1 –42 55 41.8	2.9	1.0 ± 0.4	2.3	0.9 ± 0.4	-0.15 ± 0.46	$\text{SNR}_T = 2.9$ but 60" from QSO
s4.....	0 38 17.1 –43 17 22.1	3.4	1.2 ± 0.4	2.4	1.1 ± 0.4	0.32 ± 0.44	Possibly 2 sources in HX band

NOTES.—Col. (1): *BeppoSAX* source number. Col. (2): *BeppoSAX* position (J2000); see text for positional accuracy. Units of right ascension are hours, minutes, and seconds, and units of declination are degrees, arcminutes, and arcseconds. Col. (3): Total X-ray (1.3–10 keV) SNR. Col. (4): Hard X-ray (2–10 keV) counts. Col. (5): Hard X-ray SNR. Col. (6): Hard X-ray flux. Col. (7): Softness ratio $(S-H)/(S+H)$; see § 4.2. Col. (8): Reason why source was included in the supplementary table.

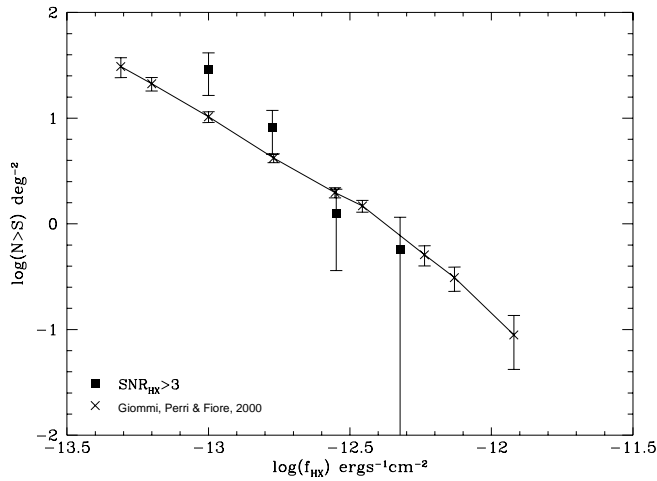


FIG. 2.—Cumulative 2–10 keV (HX) $\log N$ – $\log S$ function compared with that found by Giommi et al. (2000). Only those sources with $\text{SNR}_{\text{HX}} > 3$ are shown.

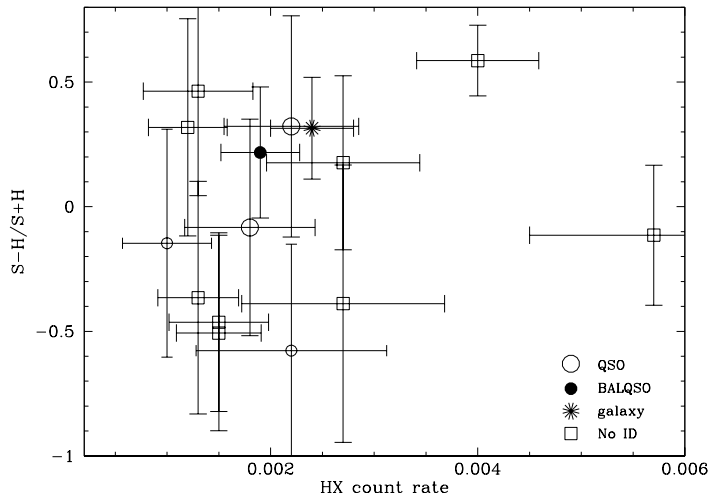


FIG. 3.—Softness ratios of the *BeppoSAX* sources as a function of HX count rate. Open circles refer to the QSOs, filled circles refer to the BAL QSO, the star refers to the galaxy and squares refer to objects without an optical ID. Smaller open circles refer to the QSO supplementary sources; see Table 3 and text.

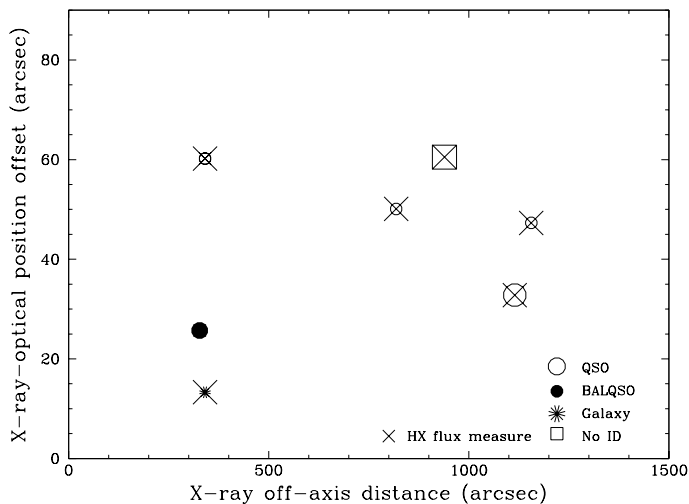


FIG. 4.—HX to optical source matching distances. The symbol size for both the MIR (15 μm) and HX fluxes represents the source flux; a larger symbol denotes a larger flux. Same object-type key as Fig. 3.

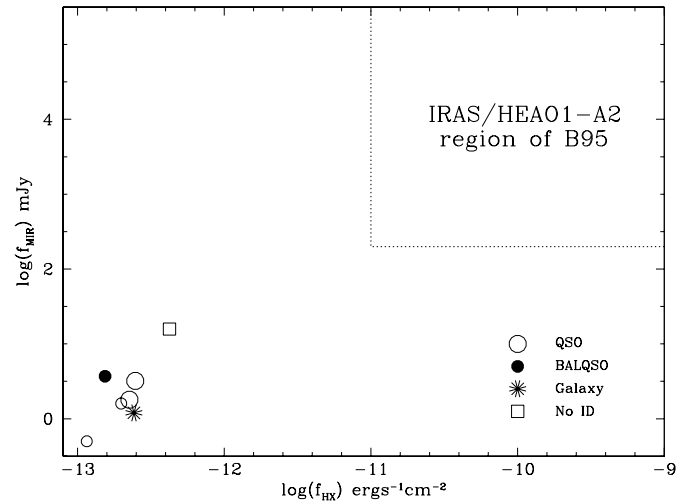


FIG. 5.—HX and MIR fluxes of the MIR-detected HX sources. Same object-type key as Fig. 3.

$\text{SNR}_{\text{HX}} > 3$ number counts of sources are reasonably consistent with those found by Giommi, Perri, & Fiore (2000); see Figure 2. We have added to the supplementary list (Table 3) two sources just below the detection threshold, with $\text{SNR}_T = 2.9$, but close ($\sim 60''$) to the position of an ELAIS 15 μm QSO. These sources are used in all further analysis.

The softness ratios of the sources were determined following the procedure of Fiore et al. (2000b), with the ratio defined as $(S-H)/(S+H)$, where S = count rate in the 1.3–4.5 keV band and H = count rate in 4.5–10 keV band; see Figure 3 and Tables 2 and 3. The distribution of ratios is consistent with that found in the *BeppoSAX* High-Energy Large Area Survey (HELLAS) (i.e., $-1 < (S-H)/(S+H) < 1$; Fiore et al. 2000b).

3.3. Positional Correlation between the *BeppoSAX* and *ISO* Sources

We have positionally correlated the HX sources to the MIR sources, finding six matches (Table 4; Fig. 4). One further match is made with a 2.6σ ISOCAM source. This source is included in further analysis, although it should be noted that this is not a significant ISOCAM detection. The separation between the X-ray and optical centroids is less than $60''$ in all cases. The optical counterparts of the ISOCAM sources have magnitudes of $R < 20$ mag. This optical magnitude limit is consistent with that found for $f_{\text{HX}} > 10^{-13}$ ergs $\text{s}^{-1} \text{cm}^{-2}$, the depth of this survey, in other HX surveys (see, e.g., Schmidt et al. 1998, Akiyama et al. 2000, and Hornschemeier et al. 2001).

The surface density of the ISOCAM sources is ~ 150 sources deg^{-2} , and therefore the chance of a misassociation with a *BeppoSAX* error box ($60''$ radius) is 13%. In previous *BeppoSAX* and *ASCA* surveys (see, e.g., Akiyama et al. 2000 and La Franca et al. 2001, in preparation), sources have been matched to optical counterparts. In these studies the high optical source density often resulted in more than one possible optical counterpart within the large *BeppoSAX* and *ASCA* error boxes. The relatively low density of MIR sources in this study results in less ambiguous source matching, although we are implicitly assuming that an ISOCAM source within a *BeppoSAX* error box is associated with the HX source. This association is expected within the unified model of AGNs (Antonucci 1993) and is found

TABLE 4
ISOCAM-DETECTED *BeppoSAX* SOURCES

Object (1)	X-Ray Position (2)	L_{HX} (ergs s^{-1}) (3)	HX-Optical Offset (arcsec) (4)	f_{MIR} (mJy) (5)	L_{MIR} (ergs s^{-1}) (6)	$f_{\text{HX}}/f_{\text{MIR}}$ (7)	Optical Position (8)	R (9)	M_R (mag) (10)	z (11)	Classification (12)
s1	0 29 57.1 -43 48 44.3	45.9	32.8	3.2	45.9	-5.5 ± 0.2	0 29 59.2 -43 48 35.3	17.4	-29.4	2.039	QSO
3	0 32 13.8 -43 32 56.9	44.6	47.3	1.8	44.4	-5.3 ± 0.1	0 32 11.1 -43 33 22.3	18.7	-24.5	0.559	QSO
s3	0 33 55.1 -42 55 41.8	45.8	60.2	0.5	45.3	-5.0 ± 0.2	0 33 52.8 -42 54 52.4	18.5	-28.9	2.584	QSO
8	0 35 11.7 -43 33 42.2	...	60.5	15.8	...	-6.0 ± 0.1	0 35 15.6 -43 33 57.7	16.4
9	0 37 08.4 -42 37 07.6	44.2	13.3	1.2 ^a	43.8	-5.1 ± 0.1	0 37 07.9 -42 37 18.6	19.4	-22.5	0.325	Galaxy
10	0 37 14.3 -42 34 55.6	45.8	25.7	3.7	46.0	-5.8 ± 0.1	0 37 15.5 -42 35 14.0	18.3	-28.7	2.190	BAL QSO
11	0 37 50.5 -43 27 53.1	44.2	50.1	1.6	44.0	-5.3 ± 0.2	0 37 53.1 -43 28 24.5	19.2	-23.1	0.398	QSO

NOTES.—Col. (1): *BeppoSAX* source number. Col. (2): *BeppoSAX* position (J2000); see text for positional accuracy. Units of right ascension are hours, minutes, and seconds, and units of declination are degrees, arcminutes, and arcseconds. Col. (3): Log hard X-ray (2–10 keV) luminosity. Col. (4): Offset from the optical source position. Col. (5): 15 μm flux density from Serjeant et al. (2000). Col. (6): Log 15 μm luminosity. Col. (7): HX/MIR flux ratio. Col. (8): Optical position (J2000). Cols. (9), (10): Apparent and absolute R -band magnitudes, respectively, from La Franca et al. (2001, in preparation). Col. (11): Redshift. Col. (12): Source classification from La Franca et al. (2001, in preparation) and Gruppioni et al. (2001, in preparation).

^a 2.6σ ISOCAM source; see § 3.3.

from both observational and theoretical tests of this model (see, e.g., B95, Granato et al. 1997, Krabbe, Boeker, & Maiolino 2001, and Alonso-Herrero et al. 2001). These X-ray and infrared observations are 2 orders of magnitude deeper than those of B95 (see Fig. 5).

3.4. Hard X-Ray Upper Limits of ISO Sources

We measured 3σ X-ray upper limits for all the spectroscopically classified MIR sources shown in Figure 1. This was accomplished by measuring the counts at an MIR source position in the same fashion as for the detected sources. The measured upper limits depend on the off-axis distance and range from 10^{-13} ergs s^{-1} cm^{-2} on-axis to $(3-5) \times 10^{-13}$ ergs s^{-1} cm^{-2} off-axis.

4. DISCUSSION

In this discussion we comment on the HX/MIR source identifications and compare the observed HX/MIR properties of the *BeppoSAX* and ISOCAM objects with those of other samples previously reported in the literature (see, e.g., B95 and Elvis et al. 1994, hereafter E94).

4.1. The Spectroscopic Object Identifications

As discussed above, we found seven MIR sources (including the 2.6σ ISOCAM source) within the 15 error-boxes ($\sim 60''$ radius, 95% significance; see § 2) of the *BeppoSAX* detections. We have obtained optical spectroscopy for six of these sources (La Franca et al. 2001, in preparation; Gruppioni et al. 2001, in preparation); see Table 4. As the optical spectroscopic campaign targeted those sources with $17 \text{ mag} < R < 20.5 \text{ mag}$, we did not obtain a spectroscopic identification for the brightest source. We find four normal broad emission-line QSOs, with $0.4 < z < 2.6$ and an L_{HX} of 10^{44} – 10^{46} ergs s^{-1} , and one broad absorption line QSO (BAL QSO) at $z = 2.2$ and $L_{\text{HX}} = 6 \times 10^{45}$ ergs s^{-1} . The 2.6σ ISOCAM source is associated with a galaxy at $z = 0.325$ and has $L_{\text{HX}} \sim 10^{44}$ ergs s^{-1} , if the association is real. Based on the distribution of object types found in other *BeppoSAX* and *ASCA* surveys (see, e.g., Akiyama et al. 2000 and La Franca et al. 2000, in preparation) we would expect to find two type 2 sources in our study. We find none, which seems surprising but is not significant (1σ) given the small number of sources. One of the two low-redshift QSOs ($z < 1$) is radio-detected (source 3: $z = 0.559$, $f_{1.4 \text{ GHz}} = 1.5 \text{ mJy}$; Gruppioni et al. 1999). BAL QSOs are rarely detected in the X-ray, particularly in the soft band, possibly because of large absorption of the X-ray emission (Gallagher et al. 1999). This is the first time a high-redshift BAL QSO has been detected in both the MIR and HX.

The unclassified source 8 is a bright optical source with an extended optical profile and is possibly detected at $90 \mu\text{m}$ ($f_{90 \mu\text{m}} = 81 \text{ mJy}$; Efsthathiou et al. 2000). Its soft HX ratio (§ 4.2) is consistent with either an AGN or a thermal bremsstrahlung-emitting source. Its high HX/MIR flux ratio (see § 4.3) suggests the former, and it is probably a nearby Seyfert galaxy.

While the detection of a normal galaxy seems surprising, many apparently normal galaxies have been detected in recent *Chandra* surveys (see, e.g., Mushotzky et al. 2000, Fiore et al. 2000a, Brandt et al. 2000, Giacconi et al. 2001, and Hornschemeier et al. 2000), although none have such a high X-ray luminosity, and many tend to have harder X-ray spectral slopes. This object has an HX/MIR flux ratio,

X-ray spectral slope, and luminosity similar to QSOs, although it lacks the typical QSO broad optical emission lines. Other interesting possibilities are that it is a BL Lac object, although the lack of radio emission and a strong Calcium break suggest against this, or a dominant cD cluster galaxy, with the X-ray emission coming from the cluster medium. The expected $\log(\text{HX}/\text{MIR})$ ratio for this latter possibility is -4.7 ± 0.4 (see, e.g., Edge & Stewart 1991 and Bregman, McNamara, & O’Connell 1990). Because of the uncertain nature of this source these possibilities are not further pursued.

4.2. Softness Ratios

We have compared the softness ratios (see Fiore et al. 2000b) with those expected for various HX SEDs; see Figure 6. The softness ratios of the QSOs, although extremely uncertain, show a variety of soft and hard sources $-0.5 < (S-H)/(S+H) < 0.5$, similar to those found in the *BeppoSAX* HELLAS survey (Fiore et al. 2000b).

4.3. The HX/MIR Flux Ratios

We have compared the observed HX/MIR flux ratios with those expected for a variety of object types. B95 statistically studied the correlation between HX and $12 \mu\text{m}$ for the *IRAS* $12 \mu\text{m}$ sample of AGNs and emission-line galaxies (Rush, Malkan, & Spinoglio 1993, hereafter RMS). The $12 \mu\text{m}$ sample represents the properties of MIR sources in the local universe, while the redshifts of these ISOCAM/*BeppoSAX* objects are substantially higher. Therefore, in order to compare this study with that of B95, it is necessary to take into account the effects of redshift, and the construction of spectral energy distributions (SEDs) is necessary. In the generation of SEDs, we have decided to take an empirical approach because of the uncertain contribution of AGNs and galactic activity at mid-IR wavelengths (see, e.g., the detailed modeling of Cen A, which is clearly an AGN although its infrared emission appears to be dominated by galactic processes; Alexander et al. 1999). To do this we first evaluated and constructed HX and infrared SEDs of QSOs, Seyfert 2’s, and H II galaxies and then normalized the X-ray

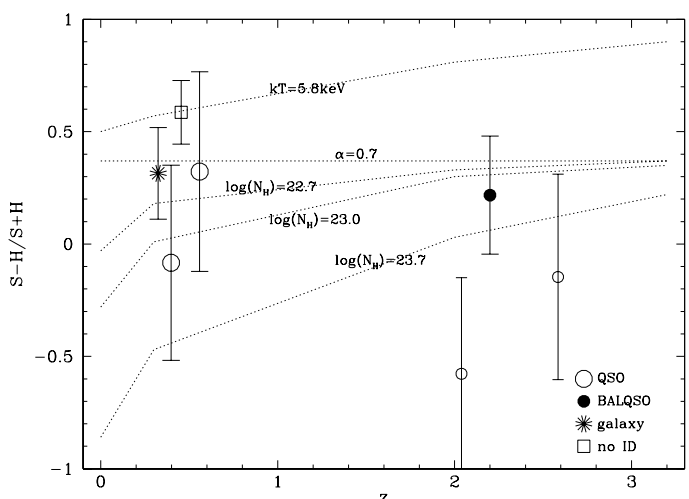


FIG. 6.—Softness ratios of the MIR-detected HX sources as a function of redshift. Dotted lines show the expected intrinsically absorbed and unabsorbed flux ratios of an AGN source and the flux ratio of a thermal bremsstrahlung-emitting galaxy or galaxy cluster. Same object-type key as Fig. 3.

SED to reproduce the HX/MIR flux ratios of the local value at $z \sim 0$, as determined by E94 for QSOs and by B95 for Seyfert 2 and H II galaxies. Only a few Seyfert 2's were detected at HX energies by B95, although the HX/MIR flux ratio distribution is very similar to those of the 16 *IRAS* 60 μm -selected, HX-detected Seyfert 2 galaxies in Alexander (2001) [$\log(\text{HX}/\text{MIR}) = -7.0 \pm 0.7$]. The B95 HX/MIR flux ratio for the H II galaxies is an upper limit.

The HX SEDs were taken from Pompilio, La Franca, & Matt (2000) for the QSOs and Seyfert 2's; the QSO SED is a two-part power law, while the Seyfert 2 SED uses this same spectrum convolved with the Seyfert 2 absorbing column density distribution found by Maiolino et al. (1998). The Seyfert 2 galaxies in the Maiolino et al. study were not MIR-selected. However, the column density distribution is very similar to that found for far-IR selected Seyfert 2 galaxies [i.e., $\log(N_{\text{H}}) \sim 22\text{--}25 \text{ cm}^{-2}$; Alexander 2001]. The H II galaxy HX SED was determined assuming a bremsstrahlung thermal spectrum with $kT = 5.8 \text{ keV}$, as found for the starburst galaxy NGC 253 (Cappi et al. 1999).

The Seyfert 2 and H II galaxy infrared SEDs were determined using the Xu et al. (1998) empirical algorithm, which takes the four *IRAS* band fluxes to predict an overall 2–120 μm SED assuming three basic components: AGN, starburst, and cirrus. The $<12 \mu\text{m}$ emission is predicted from the *IRAS* colors and produced using AGN, starburst, and cirrus observational templates that include polycyclic aromatic hydrocarbon emission and dust absorption features. The sample used to determine these SEDs was the RMS sample as classified by Alexander & Ausel (2000). These SEDs do not account for starlight, which can potentially be a large contributor for $\lambda < 7 \mu\text{m}$ and would lead to underestimates of the HX/MIR ratios. Therefore, we have only used these SEDs for $z < 1$, which is sufficient for the non-QSO sources. For the QSOs we have used the empirically determined SED of E94, which includes the contribution from starlight and gives a good match to the low-redshift, optically selected Palomar-Green (PG) QSOs (Schmidt & Green 1983). As this SED is derived mostly from low-redshift sources, we are assuming little SED evolution for $z < 3$ (see § 4.3.1 for discussion).

The HX/MIR flux ratios of the *BeppoSAX*/*ISO* sample are shown in Figure 7a. The error bars associated with the SEDs take into account the statistical spread in the HX/MIR ratios measured locally by B95. In the case of Seyfert 2's and QSOs, the effect of redshift is to increase the HX flux with respect to the MIR flux. The difference with redshift is not dramatic for either object type because the assumed HX column densities are quite low; but see § 4.3.2 for the case of a Compton thick source [$\log(N_{\text{H}}) > 24 \text{ cm}^{-2}$]. The H II galaxies are difficult to detect in the HX at any redshift but particularly at high redshift, where the HX *K*-correction is positive. In the case of a higher temperature of the X-ray emitting gas than that assumed here, the HX/MIR ratio will stay constant to higher redshifts, dropping off significantly at the exponential cutoff energy [i.e., at $z = (T_{\text{HX}}/2) - 1$, where T_{HX} is the bremsstrahlung temperature in kilo-electron volts].

The flux ratio distribution of the HX/MIR upper limits is shown in Figure 7b. The mean HX upper limit and $\log(\text{HX}/\text{MIR})$ are $3.3 \times 10^{-13} \text{ ergs s}^{-1} \text{ cm}^{-2}$ and -5.1 , respectively. To detect all the sources requires significantly deeper X-ray observations. HX observations of the northern ELAIS fields will be carried out by *Chandra* and *XMM*-

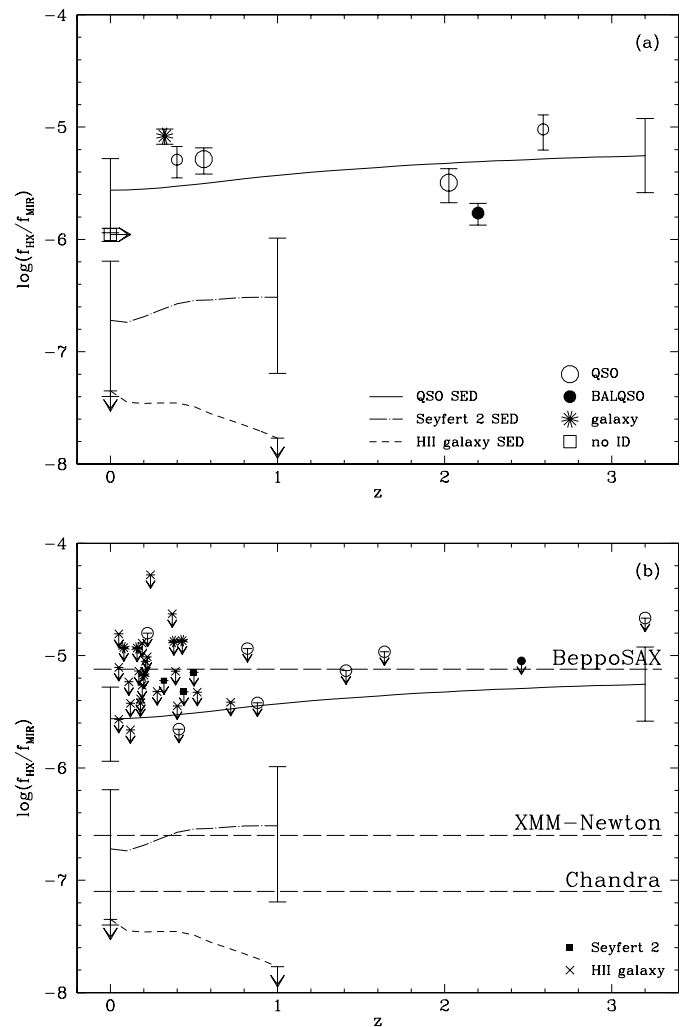


FIG. 7.—Expected $\log(\text{HX}/\text{MIR})$ flux ratios for QSOs, Seyfert 2's, and H II galaxies overplotted with (a) the MIR-detected HX sources and (b) the MIR sources with HX upper limits. Error bars are from B95 and correspond to the statistical spread in HX/MIR flux ratio for each source type. Crosses refer to H II galaxies, and filled squares refer to Seyfert 2 galaxies; see Fig. 3 for key to the other object types. The mean depth of the *BeppoSAX* and the predicted mean depths of the forthcoming *XMM-Newton* (PI, R. Mann) and *Chandra* (PI, O. Almaini) surveys of the Northern ELAIS regions are shown.

Newton to limiting fluxes of $\sim 3 \times 10^{-15}$ and $10^{-14} \text{ ergs s}^{-1} \text{ cm}^{-2}$, respectively. Assuming the mean flux and HX/MIR flux ratio of this *BeppoSAX* survey, the *Chandra* and *XMM-Newton* surveys should reach mean flux ratios of $\log(\text{HX}/\text{MIR}) \sim -7.1$ and $\log(\text{HX}/\text{MIR}) \sim -6.6$, although clearly some objects with lower ratios will also be detected. The *Chandra* survey (two ACIS-I 16' pointings) covers a small area but should detect all the AGNs and some H II galaxies within the field of view, while the *XMM-Newton* survey covers a similar area to this survey and should detect all the QSOs, most of the Seyfert 2 galaxies, and a few H II galaxies.

4.3.1. The QSOs

The majority of the HX/MIR associated sources are QSOs. The observed QSO HX/MIR flux ratios appear consistent with that of the median E94 QSO SED. The E94 UVSX sample includes 47 quasars selected to have at least 300 counts in the *Einstein* IPC and $V < 17 \text{ mag}$ to be

observable by *IUE*; 29 members are radio-quiet and 18 radio-loud. The sample is consequently biased toward objects at low redshifts (although seven objects have $z > 1$, four $z > 2$, and one $z > 3$), of moderate luminosity, and with high X-ray to optical flux ratios.

In order to increase the statistics of our comparison, we added to the MIR sample QSOs from Andreani, Franceschini, & Granato (1999) with $f_{12\mu\text{m}} > 200$ mJy and created as a comparison an optically selected sample using $12\mu\text{m}$ detections or upper limits of the optically selected PG QSOs from Sanders et al. (1989). To increase the number of objects at high redshift we have taken those objects from Neugebauer et al. (1986) with $z > 2$. We have determined which of these are BAL QSOs using the list of Junkkarinen, Hewitt, & Burbidge (1991). The data are shown in Figure 8. The mean $\log(\text{HX}/\text{MIR})$ ratios of the low-redshift QSOs ($z < 0.6$) are -5.7 ± 0.7 and -5.6 ± 0.3 for the MIR- and optically selected objects, respectively. These flux ratios are consistent with each other and with the E94 SED. This suggests that MIR-selected QSOs of $R < 20$ mag come from the same population as optically selected QSOs and that there is little SED evolution for $z < 3$.

As a further and more definitive test, we have compared the $\log(B/\text{MIR})$ ratios of all the MIR-detected QSOs in the S1 region with those of the PG QSO sample (Schmidt & Green 1983 and Sanders et al. 1989); see Figure 9. The advantage of this comparison is that we can use the full QSO set from both the ELAIS and PG surveys. The MIR QSOs are consistent with the flux ratios of the E94 SED and the PG QSOs. This further strengthens the evidence that MIR-selected QSOs of $R < 20$ mag come from the same population as optically selected QSOs.

4.3.2. The BAL QSO

Although the statistics are still poor, low-redshift BAL QSOs seem to be located in a different region of the

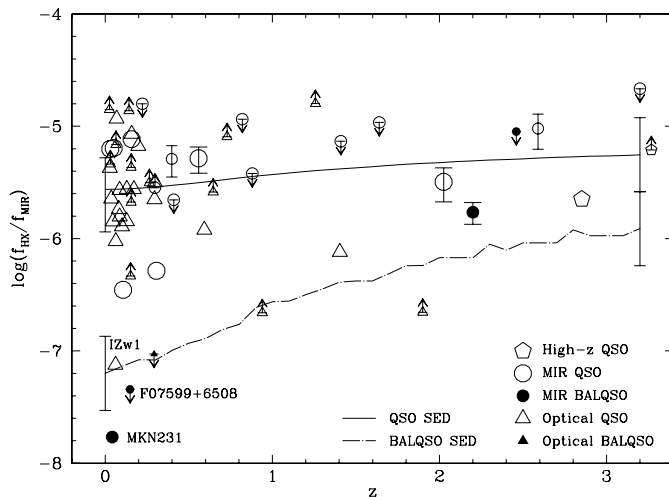


FIG. 8.— $\log(\text{HX}/\text{MIR})$ flux ratios of MIR and optically selected QSOs. The curves show the mean QSO and BAL QSO values. The statistical spread of values is calculated from the QSOs of E94. The narrow line Seyfert 1 object I Zw 1 is indicated, as well as the two nearby BAL QSOs MKN 231 and IRAS 07599+6508. See Fig. 7a for the object-type key. Additional HX data were taken from Turner & Pounds (1989), Della Ceca et al. (1990), Turner et al. (1990), Williams et al. (1992), Lawson et al. (1992), Saxton et al. (1993), Sambruna et al. (1994), Ceballos & Barcos (1996), Alonso-Herrero et al. (1997), Lawson & Turner (1997), Reeves et al. (1997), and Gallagher et al. (1999).

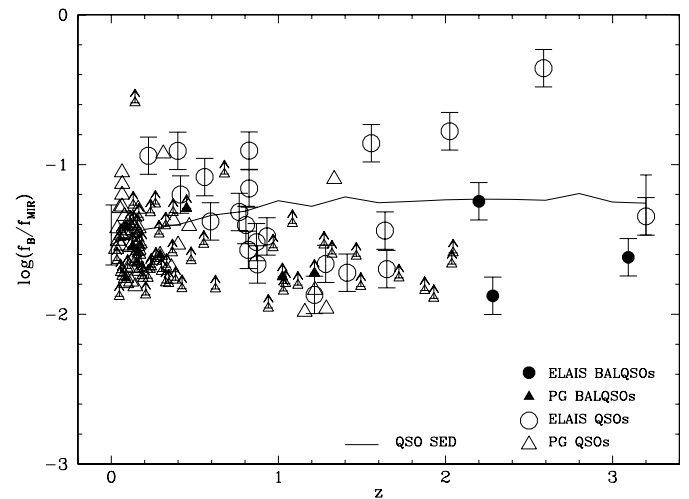


FIG. 9.— $\log(B/\text{MIR})$ flux ratios of MIR and optically selected QSOs. The curve shows the mean QSO value. The statistical spread is calculated from the QSOs of E94. See Fig. 7a for the object-type key. Data for the PG objects were taken from Schmidt & Green (1983) and Sanders et al. (1989).

HX/MIR plane than QSOs; see Figure 8. This is what would be expected from an absorbed source. The low-redshift QSO that lies close to the BAL QSOs in the HX/MIR plane, shown in Figure 8, is a narrow line Seyfert 1 galaxy (I Zw 1), an unusually red source (see, e.g., E94) which may be different from the general QSO population (see, e.g., Brandt & Gallagher 2000). Our BAL QSO has an HX/MIR flux ratio similar to that found for normal QSOs, apparently in contradiction with that found for low-redshift BAL QSOs. This difference could be due to the negative HX K -correction effect of an absorbed HX spectrum; see Figure 6. We can test whether the observed HX/MIR flux ratio is compatible with that expected for an absorbed HX source by constructing a possible BAL QSO SED. We have chosen to use the Compton thick HX spectrum of the type 2 QSO object IRAS 09104+4109 (Franceschini et al. 2000) and the QSO infrared SED of E94, normalized to the HX/MIR ratio of IRAS 09104+4109. The positive effect of redshift on the HX emission can clearly be seen (see Fig. 8), showing that a high-redshift HX absorbed source can have an HX/MIR flux ratio similar to that of an unabsorbed source. Therefore, in contrast to low-redshift BAL QSOs, high-redshift BAL QSOs should be comparatively easy to detect in the HX band, allowing a determination of their true fraction in the high- z QSO population.

5. CONCLUSIONS

We have presented shallow *BeppoSAX* observations, reaching an on-axis (~ 0.7 deg²) 2–10 keV sensitivity of $\sim 10^{-13}$ ergs s⁻¹ cm⁻², of the southern S1 region of ELAIS, reaching a $15\mu\text{m}$ sensitivity of 1 mJy. This is the first HX analysis of an ISOCAM survey. We have constructed HX and infrared SEDs to determine the expected flux ratios for QSOs and BAL QSOs up to $z = 3.2$ and for Seyfert 2 and normal galaxies up to $z = 1.0$. Our main findings are as follows.

1. We detect 13 sources with $\text{SNR} > 3$ in the 1.3–10 keV or 2–10 keV X-ray bands and a further two sources with less reliable detections that have positions close (within $\sim 60''$) to QSOs. The number densities of the $\text{SNR}_{\text{HX}} > 3$ sources

are consistent with the *ASCA* and *BeppoSAX* log N -log S function.

2. Six of these sources have reliable ISOCAM counterparts, and one further source has a less reliable (2.6σ) ISOCAM counterpart. We have optical spectroscopic classifications for six of these sources, finding four QSOs, one BAL QSO at $z = 2.2$, and one apparently normal galaxy (the 2.6σ ISOCAM source). The unclassified object has X-ray and photometric properties consistent with those of a nearby Seyfert galaxy. The galaxy has properties suggesting either an unusual QSO or a galaxy cluster.

3. The QSOs cover a wide redshift range ($0.4 < z < 2.6$) and have HX/MIR flux ratios consistent with those found for nearby *IRAS* and optically selected PG QSOs and with the QSO SED of E94. By further comparing the B /MIR flux ratios of the MIR QSOs with those of the blue-band-selected PG sample, we suggest that MIR-selected QSOs of $R < 20$ mag come from the same population as optically selected QSOs.

4. The high-redshift BAL QSO has an HX/MIR ratio similar to that of QSOs, but different from that found for low-redshift BAL QSOs. This difference can be explained as

the negative K -correction effect of an absorbed X-ray spectrum observed at high redshift. This suggests that high-redshift BAL QSOs should be comparatively easy to detect in the HX band, allowing the true fraction of BAL QSOs in the high-redshift QSO population to be determined.

We acknowledge the European Commission TMR network (FMRX-CT96-0068) for financial support and MURST Cofin 98-032 and ASI contracts for partial support. D. M. A. additionally thanks the NSF CAREERS grant AST 99-83783 for postdoctoral support. This research has made use of SAXDAS (SAX Data Analysis System) linearized and cleaned event files (Rev. 2.0), produced at the *BeppoSAX* Science Data Center, and the NASA/IPAC Extragalactic Database (NED) which is operated by the Jet Propulsion Laboratory, California Institute of Technology, under contract with NASA. We gratefully thank Belinda Wilkes, the referee, for an efficient and thorough reading of this manuscript. We further thank Cong Xu for providing the code to determine the mid-IR SEDs used in this paper and Sarah Gallagher, Ann Hornschemeier, and Niel Brandt for valuable comments on earlier drafts of this paper.

REFERENCES

- Akiyama, M., et al. 2000, *ApJ*, 532, 700
 Alexander, D. M. 2001, *MNRAS*, 320, L15
 Alexander, D. M., & Aussel, H. 2000, in *Lecture Notes in Physics 548, ISO Surveys of a Dusty Universe*, ed. D. Lemke, M. Stickel, & K. Wilke (New York: Springer), 113
 Alexander, D. M., Efstathiou, A., Hough, J. H., Aitken, D. K., Lutz, D., Roche, P. F., & Sturm, E. 1999, *MNRAS*, 310, 78
 Alonso-Herrero, A., Quillen, A. C., Simpson, C., Efstathiou, A., & Ward, M. J. 2001, *AJ*, 121, 1369
 Alonso-Herrero, A., Ward, M. J., & Kotilainen, J. K. 1997, *MNRAS*, 288, 977
 Andreani, P., Franceschini, A., & Granato, G. L. 1999, *MNRAS*, 306, 161
 Antonucci, R. 1993, *ARA&A*, 31, 473
 Barcons, X., Franceschini, A., De Zotti, G., Danese, L., & Miyaji, T. 1995, *ApJ*, 455, 480 (B95)
 Barger, A. J., Cowie, L. L., Mushotzky, R. F., & Richards, E. A. 2001, *AJ*, 121, 662
 Boella, G., Butler, R. C., Perola, G. C., Piro, L., Scarsi, L., & Bleeker, J. A. M. 1997a, *A&AS*, 122, 299
 Boella, G., et al. 1997b, *A&AS*, 122, 327
 Brandt, W. N., & Gallagher, S. C. 2000, *NewA Rev.*, 44, 461
 Brandt, W. N., et al. 2000, *AJ*, 119, 2349
 Bregman, J. N., McNamara, B. R., & O'Connell, R. W. 1990, *ApJ*, 351, 406
 Cagnoni, I., Della Ceca, R., & Maccacaro, T. 1998, *ApJ*, 493, 54
 Cappi, M., et al. 1999, *A&A*, 350, 777
 Ceballos, M. T., & Barcons, X. 1996, *MNRAS*, 282, 493
 Cesarsky, C. J., et al. 1996, *A&A*, 315, L32
 Clavel, J., et al. 2000, *A&A*, 357, 839
 Della Ceca, R., Palumbo, G. G. C., Persic, M., Boldt, E. A., De Zotti, G., & Marshall, E. E. 1990, *ApJS*, 72, 471
 Edge, A. C., & Stewart, G. C. 1991, *MNRAS*, 252, 428
 Efstathiou, A., et al. 2000, *MNRAS*, 319, 1169
 Elvis, M., et al. 1994, *ApJS*, 95, 1 (E94)
 Fabian, A. C., et al. 2000, *MNRAS*, 315, L8
 Fiore, F., La Franca, F., Giommi, P., Elvis, M., Matt, G., Comastri, A., Molendi, S., & Gioia, I. 1999, *MNRAS*, 306, L55
 Fiore, F., et al. 2000a, *NewA*, 5, 143
 ———. 2000b, *MNRAS*, submitted
 Franceschini, A., Bassani, L., Cappi, M., Granato, G. L., Malaguti, G., Palazzi, E., Persic, M., 2000, *A&A*, 353, 910
 Gallagher, S. C., Brandt, W. N., Sambruna, R. M., Mathur, S., Yamasaki, N., 1999, *ApJ*, 519, 549
 Giacomini, R., et al. 2001, *ApJ*, 551, 264
 Giommi, P., Perri, M., & Fiore, F. 2000, *A&A*, 362, 799
 Granato, G. L., Danese, L., & Franceschini, A. 1997, *ApJ*, 486, 147
 Gruppioni, C., et al. 1999, *MNRAS*, 305, 297
 Hornschemeier, A. E., et al. 2000, *ApJ*, 541, 49
 ———. 2001, *ApJ*, in press
 Junkkarinen, V., Hewitt, A., & Burbidge, G. 1991, *ApJS*, 77, 203
 Krabbe, A., Boeker, T., & Maiolino, R. 2001, *ApJ*, in press (astro-ph/0010119)
 Lawrence, A., & Elvis, M. 1982, *ApJ*, 256, 410
 Lawson, A. J., & Turner, M. J. L. 1997, *MNRAS*, 288, 920
 Lawson, A. J., Turner, M. J. L., Williams, O. R., Stewart, G. C., & Saxton, R. D. 1992, *MNRAS*, 259, 743
 Maiolino, R., Salvati, M., Bassani, L., Dadina, M., Della Cecca, R., Matt, G., Risaliti, G., & Zamorani, G. 1998, *A&A*, 338, 781
 Mushotzky, R. F., Cowie, L. L., Barger, A. J., & Arnaud, K. A. 2000, *Nature*, 404, 459
 Neugebauer, G., Miley, G. K., Soifer, B. T., & Clegg, P. E. 1986, *ApJ*, 308, 815
 Oliver, S., et al. 2000, *MNRAS*, 316, 749
 Pompilio, F., La Franca, F., & Matt, G. 2000, *A&A*, 353, 440
 Reeves, J. N., Turner, M. J. L., Ohashi, T., & Kii, T. 1997, *MNRAS*, 292, 468
 Rush, B., Malkan, M. A., & Spinoglio, L. 1993, *ApJS*, 89, 1 (RMS)
 Sambruna, R. M., Barr, P., Giommi, P., Maraschi, L., Tagliaferri, G., & Treves, A. 1994, *ApJS*, 95, 371
 Sanders, D. B., Phinney, E. S., Neugebauer, G., Soifer, B. T., & Matthews, K. 1989, *ApJ*, 347, 29
 Saxton, R. D., Turner, M. J. L., Williams, O. R., Stewart, G. C., Ohashi, T., & Kii, T. 1993, *MNRAS*, 262, 63
 Schmidt, M., & Green, R. F. 1983, *ApJ*, 269, 352
 Schmidt, M., et al. 1998, *A&A*, 329, 495
 Serjeant, S., et al. 2000, *MNRAS*, 316, 768
 Severgnini, P., et al. 2000, *A&A*, 360, 457
 Turner, M. J. L., et al. 1990, *MNRAS*, 244, 310
 Turner, T. J., George, I. M., Nandra, K., & Mushotzky, R. F. 1997, *ApJ*, 488, 164
 Turner, T. J., & Pounds, K. 1989, *MNRAS*, 240, 833
 Ueda, Y., et al. 1998, *Nature*, 391, 866
 Ueda, Y., Takahashi, T., Ishisaki, Y., Ohashi, T., & Makishima, K. 1999, *ApJ*, 524, L11
 Williams, O. R., et al. 1992, *ApJ*, 389, 157
 Xu, C., et al. 1998, *ApJ*, 508, 576